DETC2019-97534

DESIGN AND SIMULATION OF A NOVEL HIGH-SPEED OMNIDIRECTIONAL FULLY-ACTUATED UNDERWATER PROPULSION MECHANISM

Taylor Njaka
Robotics and Mechatronics Laboratory
Mechanical Engineering
Virginia Tech
Blacksburg, VA, 24061
shubh94@vt.edu

Stefano Brizzolara
ISHIP Laboratory
Aerospace and Oceans Engineering
Virginia Tech
Blacksburg, VA, 24061
stebriz@vt.edu

Pinhas Ben-Tzvi
Robotics and Mechatronics Laboratory
Mechanical Engineering
Virginia Tech
Blacksburg, VA, 24061
bentzvi@vt.edu

ABSTRACT

This paper details the design and simulation of a novel position control mechanism for marine operations or inspection in extreme, hostile, or high-speed turbulent environments where unprecedented speed and agility are necessary. The omnidirectional mechanism consists of a set of counter-rotating blades operating at frequencies high enough to dampen vibrational effects on onboard sensors. Each rotor is individually powered to allow for roll control via relative motor effort and attached to a servo-swashplate mechanism, enabling quick and powerful manipulation of fluid flow direction in a hull's coordinate frame without the need to track rotor position. The mechanism inherently severs blade loads from servo torques, putting all load on the main motors and minimizing servo response time, while exploiting consistent blade momentum to minimize the corresponding force response time. The mechanical design and kinematic analysis of each subsystem is presented, followed by kinematic and hydrodynamic analysis of the hull and surrounding fluid forces during various blade maneuvers. Special maneuvers are verified using Computational Fluid Dynamic (CFD) software. Finally, a controller is constructed with decoupled parameters for each degree of freedom.

NOMENCLATURE

α — Global surge control parameter.
β — Global yaw control parameter.
Γ — Global sway control parameter.
δ — Global roll control parameter.
θ — Blade angle along primary hull axis.
Φ — Blade attack angle.

T — Torque.
C — Cord length across an individual blade.
C_l — Lift coefficient of hydrofoil profile.
C_d — Drag coefficient of hydrofoil profile.
ρ — Mass-density of saltwater.
F — Force.
M — Mass.
M_a — Hydrodynamic added mass.
r — Radial distance from a rotor axis.
R_i — Position of blade attachment point along r.
R_o — Position of blade tip along r.
V — Velocity.
$\forall$ — Volume.

FIGURE 1: Overview of propulsion mechanism.

1

1 INTRODUCTION

Long has there been a divide between the class of submersibles composed of streamlined, torpedo-shaped vehicles (autonomous underwater vehicles (AUVs)) and that of omnidirectional or semi-omnidirectional crafts resembling the famous *ALVIN* submersible (remotely operated vehicles (ROVs)). Crafts such as the latter are capable of complex tasks involving external manipulation but are lethargic in nature and prone to flow-based disturbances, as found in shallow waters at stormy conditions or in turbulent tidal environments near artificial piers.

The growing interest in robots replacing humans in turbulent, potentially dangerous environments where precision, speed, and robustness are necessary has inspired the development of a new class of underwater robotic thrust mechanism capable of true agile omnidirectionality in a small package. Figure 1 outlines the mechanism. Challenges include but are not limited to minimizing reaction time to position disturbances, which is hindered by the delay of accelerating water and the thrust-to-mass ratio of any smaller craft attempting to actively reject disturbance. For large crafts, resilience to disturbances is inherent in vehicle mass, but fast position control is not practical. In much smaller crafts, fast position control is possible but delayed by the acceleration time of traditional cowelled thrusters, making their inherent susceptibility to disturbances difficult to combat.

Figure 2 compares the relevant characteristics of traditional AUVs [1] with those of our proposed design. These underactuated, high-speed flight vehicles are used primarily for mapping and survey applications.
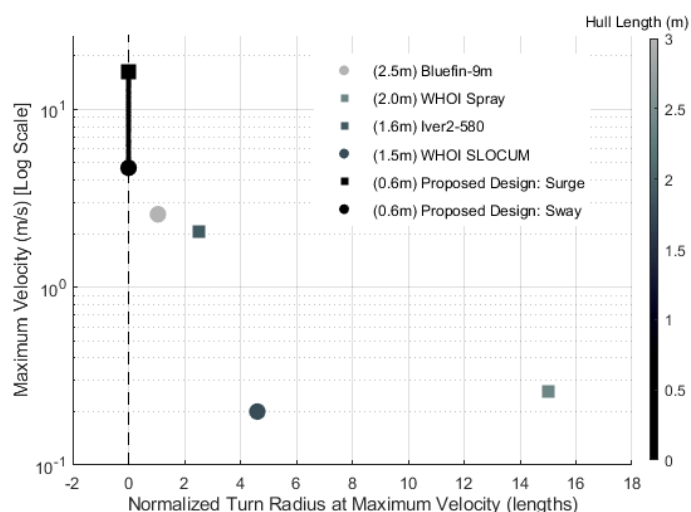

FIGURE 2: A general representation of performance characteristics of typical AUVs and comparison with proposed design. Note the zero-turning radius of the omnidirectional system.

Omnidirectional ROVs, on the other hand, are used primarily for inspection and intervention. Like the proposed design, they all share the same zero-turning radius benefit that results from their omnidirectionality, but suffer greatly in maximum speed and agility, where *agility* can be measured as the potential for instantaneous acceleration on demand. This is quantified by dividing maximum thrust by the sum of mass and added mass, where *added mass* is the virtual added mass created by fluid momentum around an accelerating body.

One small-profile omnidirectional ROV, the *MEROS*, [2] attempts to achieve adequate agility by maximizing thrust and minimizing size, but limitations using this method are realized as the craft's very thrusters greatly impact its final volume and shape profile. Figure 3 compares *mass + added mass, top speed,* and *agility* of typical omnidirectional ROVs with the proposed design characteristics. Added masses are calculated from vehicle dimensions [3, 4]. For completeness, a wide range of ROVs [5–7] is considered ranging from *heavy work-class* ROVs to *observation-class* ROVs in the size range of the proposed system:
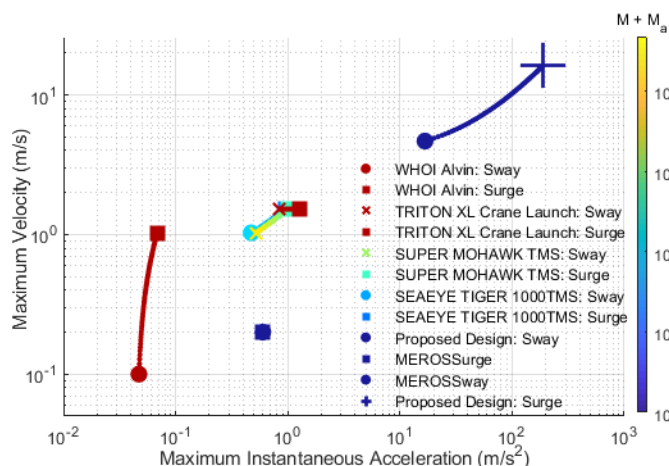

FIGURE 3: A comparison of mass, top speed, and agility-based characteristics of typical ROVs with proposed design.

Performance characteristics regarding the delay due to acceleration measurement and actuator movement are also measured and quantified. Servos used in this mechanism have an operational range of $\pm 30^o$ rotation. 0° arm positions yield 0-N force output, and full 30° deflection is calculated to yield upwards of 2500N forward thrust at 50% efficiency [see section 2.3]. KST BLS662 servos have a 0-60° time of 0.14 seconds and hence a 0-30° time of approximately 0.07 seconds. The proposed design decouples servo loads from propeller torques and forces while exploiting properties of already-moving water to kill the delay between actuator action and force output [see section 2.3]. Such high agility and reaction time may allow the craft to not only *react to* but actively *reject* various types of disturbances. Modeling said rejections is reserved for future work.

2 METHODOLOGY

We propose a small craft capable of true omnidirectionality at high speed. The proposed design consists of two sets of highly-actuated counter-rotating blades centered around a hollow tubing framework. The diameter of said tubing is chosen to allow for the safe wiring of four 670-watt brushless motors operating at maximum load. Designed mostly around pre-manufactured parts, the outer hull has a main diameter of 5.5 inches and length of 16 inches without nose attachments. Figure 4 presents an overview of the design.
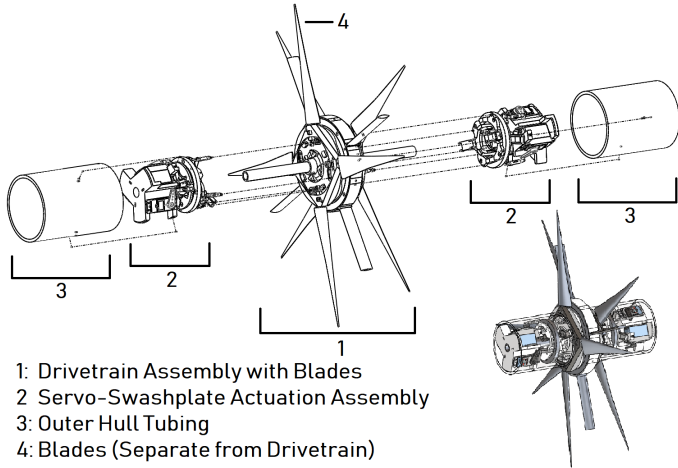
1: Drivetrain Assembly with Blades
2: Servo–Swashplate Actuation Assembly
3: Outer Hull Tubing
4: Blades (Separate from Drivetrain)

FIGURE 4: Overview of all subassemblies to be discussed.

The hull is designed to be largely free-flowing for required motor cooling and quick deployment. Such cooling is made necessary by the considerable power-to-volume ratio of the motors.
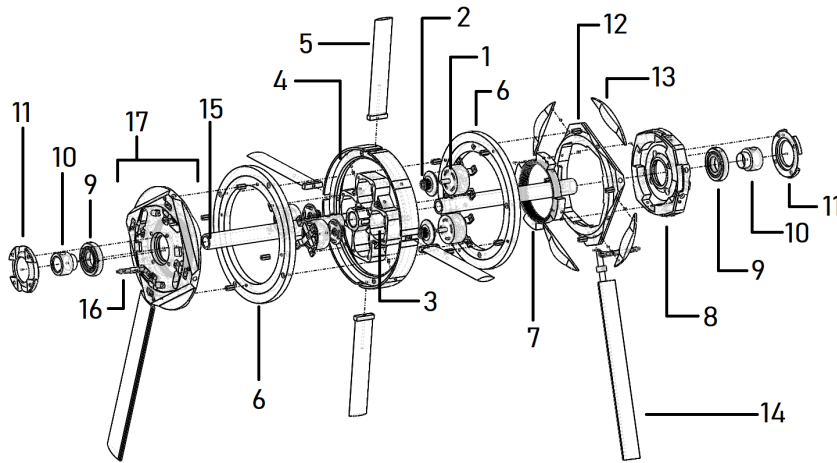
2.1 Drive Mechanism

The drive mechanism must provide independent torque to the system's rotors while locking their relative alignment and be able to support the stationary flaps responsible for limiting unwanted flow. It must also keep unwanted torques from its main bearings while staying rigid and strong at primary blade attachment points. Fortunately, geometric exploits allow for a relatively simple design solution. An engineering diagram of the entire drive-train mechanism is shown in Fig. 5.

The drivetrain is powered by two pairs of Hobbyking ST-4010-820kv brushless motors. These \$15 motors are chosen for their exceptional torque, power, size, and material-based bearing design that allows for corrosion resistance rare for motors of their size. A standard brushless motor torque-frequency linearity is constructed from data collected on Hobbyking.com regarding the motor's performance at maximum power under various loads in Fig. 6.
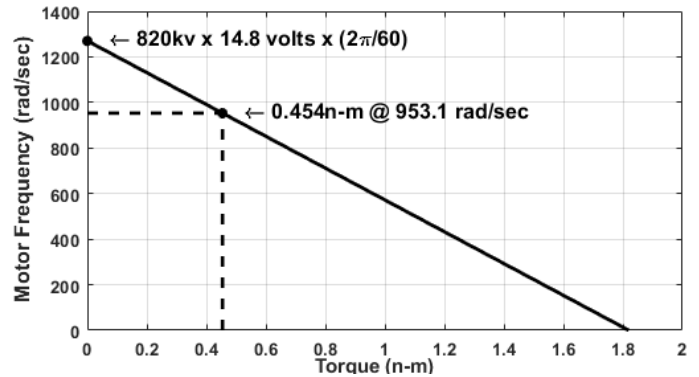
FIGURE 6: Torque-frequency chart for the Hobbyking ST-4010-820kv brushless motor.

1: HK– ST4010 Brushless Motor
2: Motor–Gear Attachment
3: Motor Holder
4: Blade–Axis Re-enforcing Susan Bearing Adapter
5: Stationary Backflow Control Flaps
6: 300mm Lazy Susan Bearing
7: Direct-Transmission Gear
8: Gear/Bearing/Pitch–Ctrl Adapter
9: Corrosion–Resistant Bearing
10: Bearing–Bk.Bone Adapter
11: Ctrl Adapter–Bearing Lock
12: Blade to Transmission Coupler and Shock Buffer
13: Shock Buffer Flow Corrector
14: Dynamic Blades (only 2 of 8 shown)
15: Structural Tubing
16: Dyn. Blade Pivot Adapter
17: Assembled Parts (7, 8, 12, 13, 14)

FIGURE 5: The exploded drivetrain of proposed design. Two dynamic blades and structural tubing are included for reference.

Copyright © 2019 ASME

From the chart, the relation between rotary frequency and output torque for each individual motor is constructed:

$$Motor\ Torque = (1270 - Motor\ Freq.)(\frac{0.454}{1270 - 953.1}) \quad (1)$$

where *Motor Torque* is measured in $n \cdot m$, and *Motor Freq.* is measured in $\frac{rad}{sec}$. From this, stall torque was calculated to be 1.82 N-m per motor, from which gears were designed to withstand the resulting 343.22N at the teeth. With a 14:132 gear-reduction from motor to rotor, and two motors per rotor, the net torque on each rotor is related to blade rotation frequency:

$$T = -0.2547\dot{\theta} + 34.3094 \quad (2)$$

where T is the *rotor* torque and $\dot{\theta}$ is the corresponding rate of rotation. Despite the trivial torque advantage of putting two motors on each rotor, the primary reason for motor pairing is to prevent gear slipping, as many of the parts in or near the motor housing are not exceptionally rigid. Figure 7 elaborates this concept while presenting a cut-out of the completed drive assembly to show where the motors are housed.
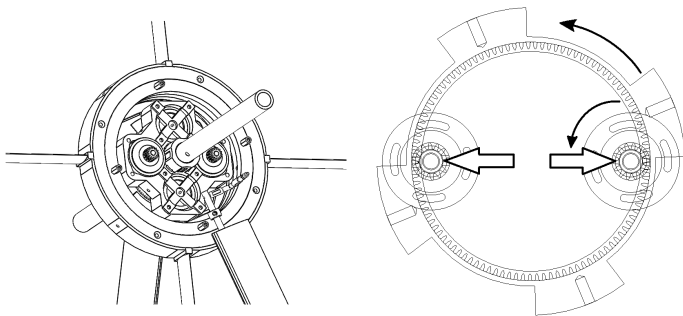

FIGURE 7: Anti-slip solution via force-balancing of twin-motor gear setup. Paired motors re-enforce each-other with respect to their shared midpoint, preventing gear slipping by greatly reducing warping in the direction of said midpoint.

Rotors are decoupled from one-another to allow for simple roll control via torque-balancing. As the effective input to each rotor is torque, not speed, roll-torque remains balanced regardless of blade parameters and relative speed, as rotation rate is simply a byproduct of the torque input. This allows for roll control via a single parameter δ, effectively decoupled from all other parameters and realized merely by varying the relative effort between the two rotors. The separate rotors are read 90% effort $\pm\delta$, where $\delta \in (-10\%, 10\%)$.

To prevent unwanted physical blade interactions, rotors are locked in alignment about their respective axes through the blade-axis re-enforcing double bearing adapter. This allows the rotors to push against one-another without touching and thereby lock axially. The same mechanism also eliminates unwanted torques on the underlying rotor bearings though the use of perpendicularly-locked standoffs, while allowing for the attachment of the stationary blades responsible for reducing unwanted flow. Figure 8 details the blade-axis re-enforcing double bearing adapter.
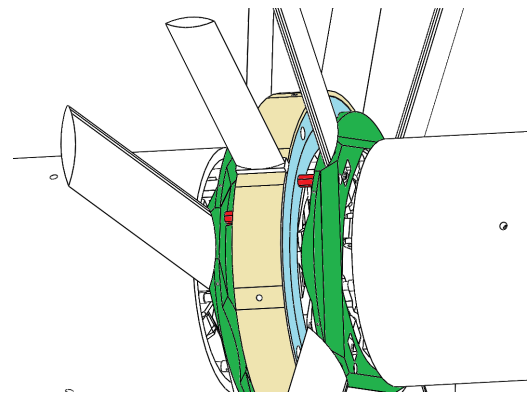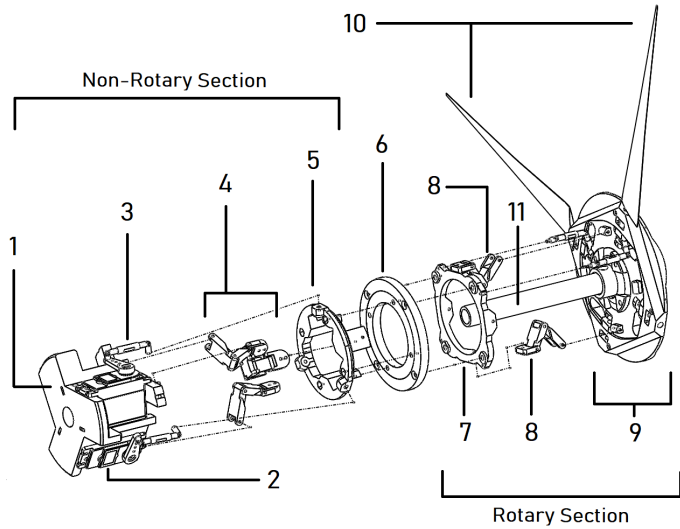

FIGURE 8: The blade-axis re-enforcing stationary flap assembly (BARSFA). The BARSFA consists of two 300mm lazy susan bearings (one shown in blue) connected to a central stationary section (yellow) from which stationary flaps can attach. Through perpendicular standoffs (red), the bearings attach directly to the aluminum blade adapters (green) that comprise the structural integrity of each rotor. Because the rotors are already locked on each-other's axes, the perpendicularity of the standoffs geometrically locks the rotors about the axis of the hull.

The central piece of the BARFSA also attaches to the underlying motor housings with four 2-inch number 6 screws. These screws prevent the back-flow flaps from drifting about θ and alleviate shear forces from the underlying rotor bearings.

2.2 Servo-Swashplate Actuator Mechanism

The design consists of two servo-swash plate actuation mechanism (SSPAM) assemblies, each connecting to its own set of four blades. Each SSPAM must quickly and accurately manipulate the pitch of spinning blades in a manner independent of rotation rate, such that blade pitch becomes some function of angle θ. This is made possible by altering the planar projection of a wide bearing assembly (swashplate) connected to the trailing edge of each blade. Figure 9 projects the expanded mechanism of a single SSPAM in its entirety.

Copyright © 2019 ASME

FIGURE 9: The servo-swashplate actuator mechanism of proposed design. There are two in total. One rotor with two blades and central tubing are shown as a visual reference.

1. Servo Housing
2. KST BLS662 Waterproof Brushless Servos
3. Servo–Swashplate Linkage
4. Non–Rotary Swashplate Hinges
5. Inner Susan–Bearing to Swashplate Adapter
6. 120mm Lazy–Susan Bearing
7. Outer Susan–Bearing to Swashplate Adapter
8. Rotary Swashplate Hinges
9. Single Rotor
10. Dynamic Blades (2 of 8 shown)
11. Stationary Structural Tubing

Three servos manipulate the forward offset and planar orientation of a lazy-susan bearing. The relative horizontal angle of the swashplate orientation varies the relative tug on the blade edges between the right and left half of the hull, while the relative vertical angle varies the tug between top and bottom. The net forward offset of the swashplate thus pushes and pulls on the average pitch of *all* blades regardless of plate orientation, controlling surge. Hinges on the servo mount connect to the stationary side of the plate mechanism and bear the torsional load of rotary friction within the plate while allowing for orientation changes. Similar hinges align the spinning rotors with the dynamic end of the plate, bearing the torsional load of the blade-pivot connectors and allowing for pivots to push rather than only pull. These dynamic hinges must attach to the plate on the same geometric plane where the stationary hinges connect to actually allow for the plate to adjust its orientation.

KST BLS662WP servos were chosen to drive this mechanism for their waterproof nature at low depths, high torque and high speed. The radial alignment of these servos to was chosen to minimize total hull radius while maintaining structural integrity, detailed in Figure 10.
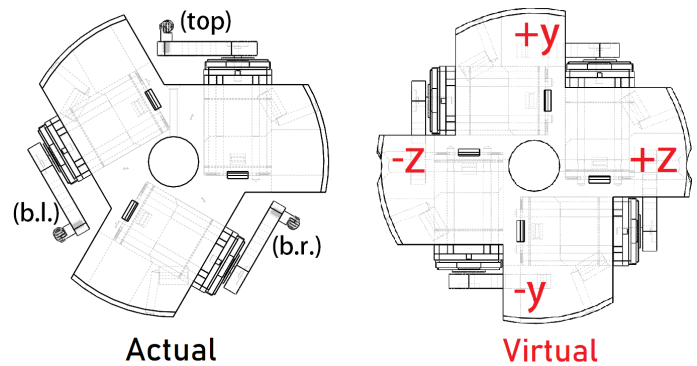

FIGURE 10: Alignment of the BLS662 servos for swashplate actuation. This configuration has a maximum diameter of 4.7 inches, allowing the hull to be composed of 5-in pvc tubing.

For explanation purposes, we will assume each SSPAA is actually composed of *four* servos: +y, -y, +z, and -z. A top servo (+y) controls the pitch of all blades passing through its (top) quadrant. A bottom servo (-y) controls the pitch of all blades passing through the bottom quadrant, while the difference between the two controls the relative thrust effort between top to bottom quadrants, thus controlling the pitch-related torque across the hull itself. Needless to say, the shared forward offset between these servos +y and -y directly affects the net forward thrust of all blades passing through quadrants +y and -y. The same principle is true regarding the difference between +z and -z servos for horizontal yaw control, as all four servos will be given the same offset control parameter. The four-servo plate-control model is trivially realized back to the three-servo model with a simple transformation, where the three servos are labeled (top), (b.r.), and (b.l.).

$$\angle(top) = \angle(+y) \qquad (3)$$

$$\angle(b.r.) = \frac{1-\sqrt{3}}{4}\angle(+y) + \frac{3-\sqrt{3}}{4}\angle(-y) + \frac{\sqrt{3}}{2}\angle(+z)$$

$$\angle(b.l.) = \frac{1-\sqrt{3}}{4}\angle(+y) + \frac{3-\sqrt{3}}{4}\angle(-y) + \frac{\sqrt{3}}{2}\angle(-z)$$

where (top) represents the uppermost servo, ($b.r.$) represents the bottom right servo, and ($b.l.$) represents the bottom left servo in a triangular orientation. A four-servo controller would use this transformation to output appropriate values to servos in the physical three-servo model.

2.3 Blade Design

The WORTMANN FX 76-100 hydrofoil profile was chosen for its bidirectionality, wide linear regime, and exceptional lift/drag performance. Its lift-to-drag (C_l to C_d) coefficient ratio peaks at an attack angle of 6.5 degrees, where $C_l = 0.75$ and $C_d = 0.018$ [8]. Figure 11 shows the dimensionless FX76-100 profile.
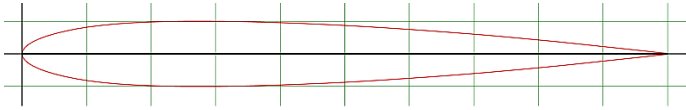
FIGURE 11: The WORTMANN FX 76-100 bi-directional hydrofoil profile. This hydrofoil peaks in lift/drag at 6.5 degrees, where it is expected to produce maximum thrust in all fluids.

Physical design constraints render R_i equal to 0.09m, and the base cord-length $C(R_i) \equiv C_i$ equal to 0.05m. The hydrofoil attack angle ϕ is set to 6.5 degrees, where the thrust is expected to peak if limited by torque. The mechanical torque limitations are detailed in Eqn.(2). Through MATLAB, many combinations of C(r), R_o, and $\dot{\theta}$ are tested and their thrusts evaluated, and it quickly becomes apparent the best C(r) cord-length function that results in the highest valid thrust outputs is a linear decrease in cord length from C_i to as small a length as possible at the blade tip C_o. C_o is then set to 2mm (0.002m).

With C(r) now fully defined, combinations of R_o and $\dot{\theta}$ which maximize thrust are plotted using the Eqn.(2) torque constraint and hydrofoil properties. Figure 12 details the output.
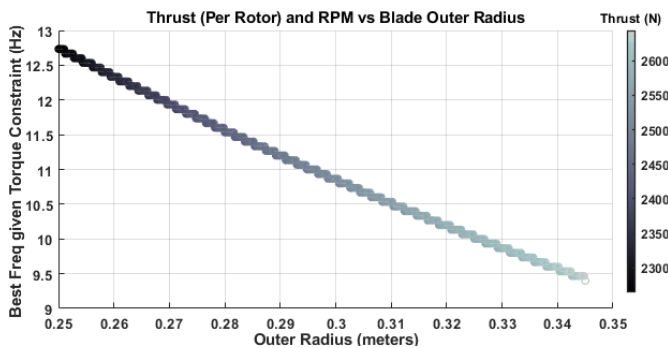

FIGURE 12: Rotor performance given torque constraints as a function of frequency. Thrust is only evaluated and plotted if mechanical torque limitations are satisfied. 10Hz equates to 80Hz blade overlap frequency.

Hydrofoils such as the WORTMANN FX 76-100 have a property where it takes little to no torque to rotate them about some pivot point approximately 30% up the cord length, for small attack angles ϕ in the linear regime of the foil under load [9]. Figure 13 outlines the final blade design, showing where the hydrofoil pivots to exploit the pivot-torque property and minimize force on the actuating servos.

3 ACTUATION AND MANEUVERABILITY

We revert back to the four-servo model detailed in Section 2.2 for explanation purposes. Recall that each servo in this model directly controls the pitch of blades passing through its particular
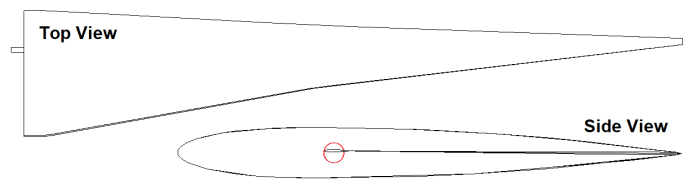

FIGURE 13: Final blade profile of proposed design. The cord profile (top view) of the blade is made mostly triangular to maximize thrust according to MATLAB simulation, while all cross-sections pivot about a point approximately 30% down the cord line, alleviating flow-based back-force on the servos that actuate them.

quadrant, and all four servos are given the same offset parameter. Servos $\pm z$ control the craft's behavior in the horizontal plane, while servos $\pm y$ control the craft's behavior in the vertical plane. Furthermore, any subsequent horizontal-plane control parameter that is fed to servo $+z$ as a value N will be fed to servo $-z$ as the value $-N$. The same holds true for servos $\pm y$. Notice how the centroid of the swashplate connecting the four servos never shifts for such control inputs, completely decoupling inputs unique to the xy plane from inputs unique to the xz plane. A two-dimensional model can then be constructed that depicts how the vehicle behaves in the isolated xy plane.

3.1 Control Modes and Superposition

Viewing the entire hull from the side, we explore the interactions between actuators $+y$ and $-y$ on the right and left rotors. As previously discussed, Figure 14 now illustrates the two-dimensional surge maneuver.
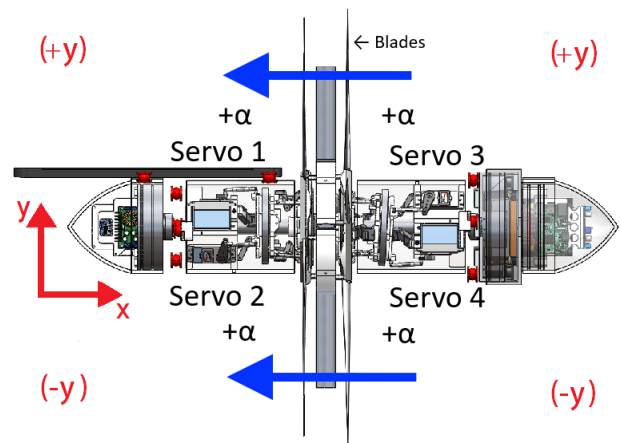

FIGURE 14: Two-dimensional surge maneuver on ROV implementation with tether-power conversion unit, side-scan sonar, and other electronics. Surge parameter α is fed to all servos in the proposed design, causing a positive thrust in $\hat{x}$. The resulting flow is represented with blue arrows.

Likewise, Fig. 15(a) illustrates the yaw maneuver in two dimensions and specifies control inputs governed by global vertical yaw parameter β. Yaw inputs $-\beta$, β, $-\beta$, and β are fed directly to servos 1, 2, 3, and 4, respectively. Control parameters can be superimposed to achieve multiple maneuvers simultaneously, as they do not inherently interfere with each other [10] due to the rigid nature of the blades. Figure 15(b) details how control parameters α and β would be fed to servos 1-4 to execute two independent control modes at once.
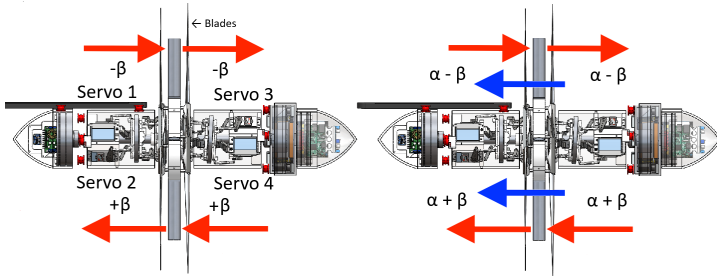

FIGURE 15: (a, left) Two-dimensional yaw maneuver on ROV implementation. (b, right) Two-dimensional superposition of yaw and surge maneuvers. Servos are fed the summation of different control parameters. Arrows conceptualize flows due to α and β. The proposed design allows superposition of *all* control parameters simultaneously, as they do not fundamentally interfere with each others' functionality [10].

A third control parameter Γ is proposed for sway. Such a maneuver is made possible from the rigid nature of the blades and durable alignment-locking of the rotor axes. Like those of other plane-oriented control parameters, sway-related actuator inputs do not shift swashplate centroids, maintaining isolation between all vertical and horizontal-plane maneuvers. Figure 16 elaborates the principle behind this sway maneuver mechanism.
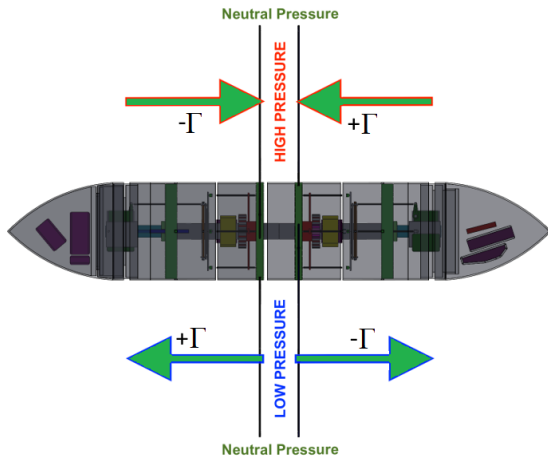

FIGURE 16: Two-dimensional sway maneuver on simplified ROV implementation. Sway parameters $-\Gamma$, Γ, Γ, and $-\Gamma$ are added to servo inputs 1, 2, 3, and 4, respectively.

Net inputs to virtual servos 1-4 are then respectively α-β-Γ, α+β+Γ, α-β+Γ, and α+β-Γ. We set $\alpha \in (-10^o, 10^o)$, $\beta \in (-10^o, 10^o)$, and $\Gamma \in (-10^o, 10^o)$ such that $|\alpha + \beta + \Gamma| < 30^o$, the physical control limit of each servo. The issue regarding unwanted flow across the pressure differential in the sway maneuver is presented and solved in Fig 17.
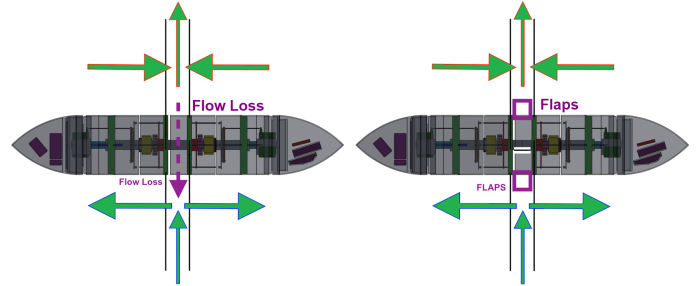

FIGURE 17: Flow loss due to pressure differential across space between rotors. Unwanted flows are minimized through the *BARSFA* flaps described in Section 2.1.

3.2 Simulated Sway Performance

It is important to note that the full computational fluid dynamic (CFD) modeling of roll, surge, and yaw maneuvers was determined to have lesser relevance in testing practicality of the proposed mechanism. For example, in no reasonable scenario will pulling *all* blade pitches forward *not* cause the craft to surge as intended if properly programmed with servo limits considered. Yaw and roll control parameters are similarly straightforward. These maneuvers are practically identical to the operational foundation of all dual-blade rotorcraft [10]. The omnidirectionality of the proposed mechanism comes from its unique ability to potentially *sway* quickly, allowing it to move in any orientation at speeds only slightly approachable by AUV's. Aside from possibly extraordinary surge and yaw properties, the *sway* maneuver sets the craft aside from ROV's.

Due to particularly small geometries near the blade tips, and highly-pronounced torque implications that result from any reduced accuracy, pure CAD-based CFD propeller simulations have proven to be impractical and unwieldy, where a highly-accurate simplified approach to blade simulation should be taken instead. First, we define two cylindrical regions with the same outer radii R_o as our rotor. A central cutout of radius R_i is assigned to each region, and each cylinder is given a thickness equal to the maximum blade projection possible in the direction of the hull axis. As these disks represent the regions the blades will cover along their rotation, we then implement the relative force intensity of thrust as a function of position that we derived from hydrodynamic properties of the finalized blade design.

To actually measure the force output from the simulation, we define a virtual box [11] of side-length L around the craft in CFD. All sides of this virtual box have walls of very small but finite volume and are comprised of CFD cells. The y-force due solely to fluid momentum on each wall of the box in the direction is

$$F_{wall} = \sum_{all\ cells} \frac{\rho \forall_{cell}|V_{\vec{n}}||V_y|L^2}{\forall_{wall}} \tag{4}$$

where $V_{\vec{n}}$ is the velocity component normal to the outer box surface, and *all* sources of fluid momentum in the system are contained within the virtual box. The two sides of the box aligned with $\pm y$ present an added force component due to the pressure difference between them, which is trivially calculated by multiplying the mean pressure difference by L^2. Figure 18 details a virtual box and the results of the sway maneuver test.
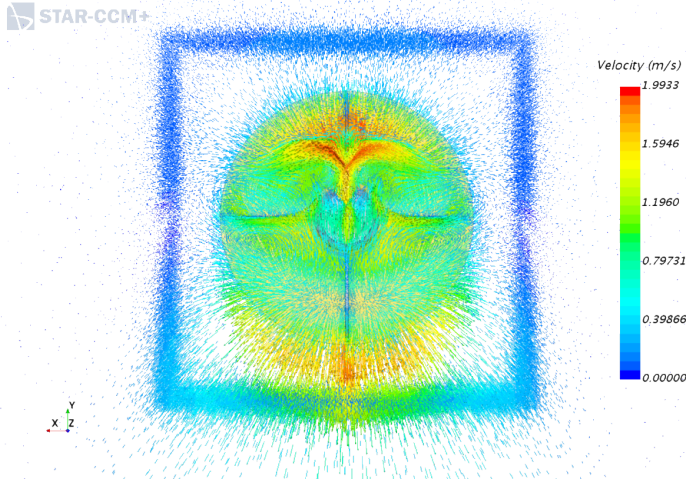

FIGURE 18: Vector graphic of dual-disk simulation with the virtual box for the sway maneuver.

Total sway forces measured suggest the craft can output between 10% and 20% force in the sway direction that it can in the surge direction.

3.3 Implementing Controller Modes

We now have enough information to construct a rudimentary 6-DOF controller with unique parameters for each DOF. Open-loop control parameters are mapped to forces and torques:

$$\begin{bmatrix} F_x \\ F_y \\ F_z \\ T_x \\ T_y \\ T_z \end{bmatrix} = \begin{bmatrix} F_{surge} \\ F_{sway} \\ F_{heave} \\ T_{roll} \\ T_{yaw} \\ T_{pitch} \end{bmatrix} = \begin{bmatrix} 250 & 0 & 0 & 0 & 0 & 0 \\ 0 & 50 & 0 & 0 & 0 & 0 \\ 0 & 0 & 50 & 0 & 0 & 0 \\ 0 & 0 & 0 & 6.2 & 0 & 0 \\ 0 & 0 & 0 & 0 & 22.5 & 0 \\ 0 & 0 & 0 & 0 & 0 & 22.5 \end{bmatrix} \begin{bmatrix} \alpha \\ \Gamma_y \\ \Gamma_z \\ \delta \\ \beta_y \\ \beta_z \end{bmatrix} \begin{matrix} |\alpha|<10^o \\ |\Gamma_y|<10^o \\ |\Gamma_z|<10^o \\ |\delta|<10\% \\ |\beta_y|<10^o \\ |\beta_z|<10^o \end{matrix}$$
$$\tag{5}$$

We implement knowledge that the static Rotor Effort offset rests at 90% and all servos have a 90° offset, and that all (-x) servos are fed the negative of their respective control angles as shown in Figure 14. All control parameters are thus mapped to physical actuator commands:

$$\begin{bmatrix} +x\ Rotor\ Effort \\ -x\ Rotor\ Effort \\ +x\ \text{"top"}\ ServoAngle \\ +x\ \text{"b.r."}\ ServoAngle \\ +x\ \text{"b.l."}\ ServoAngle \\ -x\ \text{"top"}\ ServoAngle \\ -x\ \text{"b.r."}\ ServoAngle \\ -x\ \text{"b.l."}\ ServoAngle \end{bmatrix} = \begin{bmatrix} 90\% \\ 90\% \\ 90^o \\ 90^o \\ 90^o \\ 90^o \\ 90^o \\ 90^o \end{bmatrix} + \begin{bmatrix} 0 & 0 & 0 & -1 & 0 & 0 \\ 0 & 0 & 0 & 1 & 0 & 0 \\ 1 & 0 & -1 & 0 & 0 & -1 \\ 1 & \frac{\sqrt{3}}{2} & \frac{1}{2} & 0 & \frac{\sqrt{3}}{2} & \frac{1}{2} \\ 1 & -\frac{\sqrt{3}}{2} & \frac{1}{2} & 0 & \frac{\sqrt{3}}{2} & \frac{1}{2} \\ -1 & 0 & -1 & 0 & 0 & 1 \\ -1 & \frac{\sqrt{3}}{2} & \frac{1}{2} & 0 & -\frac{\sqrt{3}}{2} & \frac{-1}{2} \\ -1 & \frac{\sqrt{3}}{2} & \frac{1}{2} & 0 & \frac{\sqrt{3}}{2} & \frac{-1}{2} \end{bmatrix} \begin{bmatrix} \alpha \\ \Gamma_y \\ \Gamma_z \\ \delta \\ \beta_y \\ \beta_z \end{bmatrix}$$

4 CONCLUSIONS AND FUTURE WORK

This paper presented the design and simulation of a small omnidirectional vehicle with speed and agility sufficient enough to work in turbulent environments inaccessible to traditional craft, as would be seen in many shallow environments that require inspection. Bi-directional blades were designed to maximize thrust while staying long enough to exploit properties emerging from continuous counter-rotation and potentially generate lateral thrust as its own control parameter. This lateral control parameter was verified using STARCCM+ CFD software and all open-loop control modes were shown to be decoupled from one another. Finally, a basic open-loop controller was designed linking all open-loop control parameters for surge, yaw, and roll to desired output forces and moments. These control parameters were also mapped to physical actuator outputs.

Future work involves simulation of closed-loop, inertia-based feedback performance to gauge rejection of heavy external fluid disturbances. The work also includes fabrication of a micro or full-scale model to accurately assess sway-performance, delays, and possibly robust positioning in the presence of turbulance with some primary oscillation direction.

REFERENCES

[1] McColgan, J., and McGookin, E., 2016. "Coordination of Multiple Biomimetic Autonomous Underwater Vehicles Using Strategies Based on the Schooling Behaviour of Fish". *Robotics,* **5**(1), 1, p. 2.

[2] Chikh, L., 2013. *MEROS Project Technical Advances in Modeling and Control.* No. February.

[3] Eidsvik, O. A., and Schjølberg, I., 2016. "Determination of Hydrodynamic Parameters for Remotely Operated Vehicles". In Volume 7: Ocean Engineering, NTNU, p. V007T06A025.

[4] Kepler, M. E., Pawar, S., Stilwell, D. J., Brizzolara, S., and Neu, W. L., 2018. "Assessment of AUV Hydrodynamic Coefficients from Analytic and Semi-Empirical Methods". In OCEANS.

[5] Media Downloads — Oceana Subsea Independent ROV Services.

[6] Maloof, R. H., Forrester, N. C., and Albrecht, C. E., 1986. "A Brushless Electric Propulsion System for the Research Submersible Alvin". In IEEE/MTS Oceans '86.

[7] Wernli, R., 1999. "The Present and Future Capabilities of Deep ROVs". *Marine Technology Society Journal,* **33**(4), 1, pp. 26–40.

[8] WORTMANN. WORTMANN FX 76-100 (fx76100-il).

[9] Hoerner, S. F., Michel, W. H., Ward, L. W., and Buermann, T. M., 1954. Hydrofoil Handbook. Volume I, Design of Hydrofoil Craft.

[10] Service., U. S. F. S., 1978. *Basic helicopter handbook.* Superintendent of Documents.

[11] Botella, O. N. U., and Cheny, Y. N. U., 2010. "An Overview of the LS-STAG Immersed Boundary Method for Viscous Incompressible Flows". In Computational Fluid Dynamics.